Combined in Situ and Time-Resolved SANS and SAXS Studies of Chemical Reactions at Specific Sites and Self-Assembling Processes of Reaction Products: Reduction of Palladium Ions in Self-Assembled Polyamidoamine Dendrimers as a Template

Hirokazu Tanaka,[†,‡] Satoshi Koizumi,*[,†] Takeji Hashimoto,*[,†,‡] Hideaki Itoh,[‡] Masahide Satoh,[‡] Kensuke Naka,[‡] and Yoshiki Chujo[‡]

Advanced Science Research Center (ASRC), Japan Atomic Energy Agency (JAEA), Tokai, Ibaraki 319-1195, Japan, and Department of Polymer Chemistry, Graduate School of Engineering, Kyoto University, Kyoto 615-8510, Japan

Received December 21, 2006; Revised Manuscript Received March 22, 2007

ABSTRACT: We reported the reduction process of palladium(II) acetate, $Pd(OAc)_2$, and the self-assembling process of the resulting palladium atoms, Pd(0), into nanoparticles in the presence of a first-generation polyamidoamine dendrimer (G1-NH_2) in nonaqueous solution. The process was induced by mixing the two solutions (A) $Pd(OAc)_2$ dissolved in *N*,*N*-dimethylformamide (DMF) and (B) G1-NH_2 dissolved in methanol, under the specific condition of $r \equiv [Pd(OAc)_2]/[-NH_2] = 3.3$, where $[-NH_2]$ is the molar concentration of the primary amine groups in the dendrimer in the reaction solution. The reaction and reaction-induced self-assembling process were explored in situ by means of a combined time-resolved method of small-angle neutron scattering and small-angle X-ray scattering. The method revealed the time evolution of a series of self-assembling processes occurring in the system. (a) The dendrimer molecules and $Pd(OAc)_2$ first self-assemble themselves rapidly into spherical aggregates with an average radius of ∼30 nm after onset of the reaction, and thereafter their size was kept almost constant. (b) Inside the aggregates, which serve as a template for the reaction, the reduction of $Pd(OAc)_2$ to Pd(0) and their self-assembly into Pd nanoparticles with an average radius of 0.4−1.7 nm proceeds gradually with time over 12 h. The following factors are proposed to be important for understanding the series of self-assembling processes: (i) the relative strength of interactions among the constituents $Pd(OAc)_2$, G1-NH_2, DMF, and methanol and (ii) the reduction of $Pd(OAc)_2$ with methanol as a weak reducing agent and the self-assembly of the reduction products of Pd(0) in the templates.

1. Introduction

In this paper, we aim to investigate the in situ, real-time reduction process of metal ions into metal atoms and a self-assembling process of metal atoms into nanoparticles in a nonaqueous solution, which contains the first-generation poly(amidoamine) (PAMAM) dendrimers (designated hereafter G1-NH_2), by means of a combined SANS (small-angle neutron scattering) and SAXS (small-angle X-ray scattering) method, together with a real-space analysis by transmission electron microscopy (TEM). It is worth noting here that the self-assembly of G1-NH_2 rather than an isolated G1-NH_2 turns out to provide a template where the chemical reaction and the reaction-induced self-assembly of reaction product take place, as will be clarified later in this paper. This study may be considered as an interdisciplinary one between chemistry (a chemical reaction involving reduction of metal ions) and physics (self-assembly of metal nanoparticles).

Recently, wide-ranging studies on metal nanoparticles have been reported from the viewpoints of both fundamental science and practical interests.[1−4] Metal nanoparticles are regarded as promising candidates for novel functional materials, such as optoelectronic devices and catalysts, because of their small size[5,6] and large specific surface area. However, due to the increased surface area, they easily aggregate themselves to form larger clusters. Hence, their surface should be protected against clustering and agglomeration by stabilizers, such as polymers,[7−13] surfactants,[14] ligands,[15] and so on.

Dendrimers also have been attracting much attention as useful stabilizers of metal nanoparticles in solutions,[16−27] since the first successful report by Crooks and his co-workers in 1998.[16] Most of these studies deal with the reduction in a solution where dendrimers are molecularly dissolved, essentially isolated from one another in solution, and metal ions are encapsulated in the interior space of single dendrimers. The ions are reduced to metal atoms which self-assemble into a metal nanoparticle within the single dendrimers. In this sense dendrimers provide a special site or field for the chemical reaction and reaction-induced self-assembly of the reaction products and, hence, they serve as a template. One of the merits of using dendrimers as the template as described above is that size of metal nanoparticles can be controlled simply by changing the generation of dendrimer, *GN*.

The system to be explored in this work is the same as that described above from the viewpoint that it is composed of dendrimers, metal ions, reducing agent, and solvent but is quite different from the viewpoints of (i) the nature of local interactions among the components described above, (ii) the ratio *r* of the molar concentration of metal ions $[M^{n+}]$ to that of the peripheral functional group of the dendirmer [X], defined by $r = [M^{n+}]/[X]$, (iii) the reducing power of the reducing agent, and (iv) the generation number of the dendrimer *GN* used for experiments. As a consequence of these differences, our system forms an association of dendrimers rather than isolated single dendrimers in solution. We focus on the self-assembling mechanism of the dendrimer association and on the role of the dendrimer association as a template for the reduction reaction, which have not been explored so far, to the best of our

[†] Japan Atomic Energy Agency.
[‡] Kyoto University.

10.1021/ma062930u CCC: $37.00
Published on Web 05/12/2007

Table 1. Comparison of Experimental Conditions Employed in the Previous Studies and This Study

	GN[a]	reacn medium	metal complex	reducing agent	*r*[b]
past studies	4−10	aqueous soln	K_2PdCl_4, $HAuCl_4$	$NaBH_4$	<1
this study	1	methanol/DMF (10/1, v/v)	$Pd(CH_3COO)_2$	methanol	3.3

[a] Generation of dendrimers. [b] $r \equiv [M^{n+}]/[-NH_2]$ or $[M^{n+}]/[-OH]$.

knowledge. Some outstanding differences to be noted are summarized in Table 1. We shall describe below the differences one by one.

First, we wish to point out the differences in *GN* and *r*. Most of the past studies utilized dendrimers with $GN \geq 4$ and a small concentration $[M^{n+}]$, corresponding to $r \leq 1.0$. In contrast, this work deals with dendrimers with $GN = 1$ and a large concentration $[M^{n+}]$, as characterized by $r = 3.3$. There are some important differences between low-generation dendrimers and high-generation dendrimers. In addition to the obvious size difference, the low-generation dendrimers are more flexible, having greater conformational freedom than the higher generation dendrimers. This favors a trend for interdendrimer aggregations mediated by attractive interactions between metal ions and/or salts with the peripheral functional groups of the dendrimer. A higher value for *r* also favors this trend. We aim to explore the effects of this trend on associations of dendrimers and reduction processes of metal ions and/or salts.

Second, we wish to stress the differences in the reaction medium and the metal complex. In past studies, water has been almost exclusively used as a solvent, and metal complexes soluble in water have been employed to prepare homogeneous solutions of dendrimers, free from aggregations. In this study, however, we used a nonaqueous system composed of a mixture of methanol and DMF as the solvent. The metal complex used in this work is difficult to be dissolved in methanol but is soluble in DMF. These two differences may induce significant changes in the local interactions of constituent components in the reaction systems and hence may cause dramatic changes in the reduction processes of metal ions and also the self-assembling processes of metal nanoparticles.

In addition, we wish to note the difference in reducing agents. Though almost all the previous studies have used relatively strong reducing agents such as sodium borohydride ($NaBH_4$), hydrogen, ascorbic acid, etc., in this study we introduced no additional reducing agents other than methanol, which works as a solvent and as a relatively weak reducing agent as well. This will cause the reduction of metal ions or salts to be much slower, the rate of which may compete with that of the self-assembly of the dendrimers mediated by metal ions or salts as binders for interdendrimer cross-linkings. If the reduction rate is faster than the assembly rate, the dendrimer association may not be formed. If the latter is faster than the former, dendrimer association may occur. The weak reducing power of methanol may not reduce the parts of $Pd(OAc)_2$ molecules or ions which strongly bind with the peripheral functional groups of the dendrimers, which in turn enhance the chemical stability of the dendrimer associations. If the dendrimer association comes into play, the association itself serves as templates for the chemical reaction. This situation may also make an in situ observation of the reduction process much more feasible.

So far, reduction processes of metal ions and the resulting metal nanoparticles have been investigated mainly by transmission electron microscopy (TEM),[1−4,7−29] UV−vis spectroscopy,[14] small-angle X-ray scattering (SAXS),[11,13,28] and small-angle neutron scattering (SANS).[21,22] However, the TEM analysis is basically not suitable for an in situ observation of reduction process of metal ions. UV−vis spectroscopy has been a powerful tool for in situ observation and provides much information on local interactions such as coordination states of metal ions and their surroundings. However, it is impossible to directly extract information on the shape and/or size of metal nanoparticles. In contrast, the SAS (small-angle scattering) methods enable us to evaluate both shape and size. In fact, Amis and co-workers showed the SANS and SAXS profiles for Au nanoparticles in the template of PAMAM dendrimers with *GN* between 2 and 10 in aqueous solutions.[22] However, the measurements were performed only before and after the reduction. Therefore, the process and mechanism of formation of the metal nanoparticles in the templates have not been well explored at all.

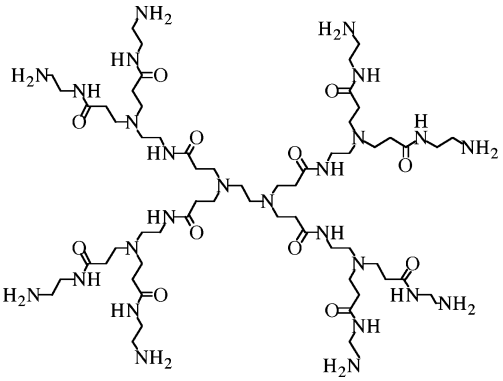

Figure 1. Chemical structure of G1.0 PAMAM dendrimer (G1-NH_2).

Scheme 1. Experimental Procedure To Prepare Palladium Nanoparticles

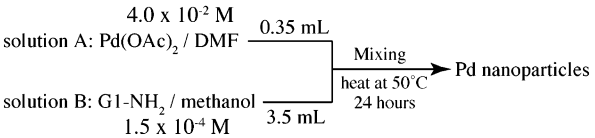

In this work we try to explore both the association process of the G1-NH_2's themselves and the reduction process of Pd ions into Pd atoms and the self-assembling process of Pd nanoparticles. It is important to note that this work is an extension of earlier studies reported by Naka et al.[26] on the self-assembly of Pd nanoparticles and dendrimer aggregates in the system comprising G1-NH_2, $Pd(OAc)_2$, and methanol.

2. Experimental Methods

2.1. Sample Specimens. We used $Pd(OAc)_2$ dissolved in DMF and G1-NH_2 (hereafter we denote the *n*th generation of PAMAM dendrimers having amine groups as the peripheral functional groups as "*GN*-NH_2") dissolved in deuterated methanol. The use of deuterated methanol is to enhance the scattering contrast for dendrimers, $Pd(OAc)_2$, and Pd nanoparticles as well as to reduce the incoherent scattering intensity. Again we like to note that $Pd(OAc)_2$ is hardly soluble in methanol, while G1-NH_2 dissolves well in both methanol and DMF. In Figure 1, we present the chemical structure of G1-NH_2, which contains 8 primary amine groups, 6 tertiary amine groups, and 12 amide groups, whose strength of attractive interactions with $Pd(OAc)_2$ decreases in the order of primary amine groups, tertiary amine groups, and amide groups.

2.2. Reduction of $Pd(OAc)_2$ (Synthesis of Pd Nanoparticles). The procedure for synthesis of Pd nanoparticles is shown in Scheme 1. The two dilute solutions of $Pd(OAc)_2$ in DMF (4.0×10^{-2} M) (denoted as "solution A") and G1-NH_2 in deuterated methanol (1.5×10^{-4} M) (denoted as "solution B") were independently prepared. We mixed 0.35 mL of solution A and 3.5 mL of solution B and

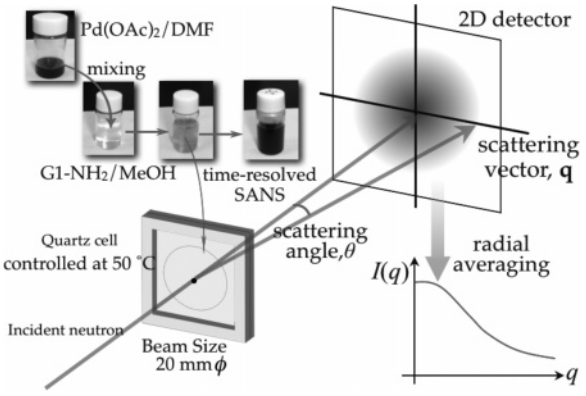

Figure 2. Experimental setup for the time-resolved SANS measurement.

heated the mixture at 50 °C for 24 h. After the mixing, methanol acts as a reducing agent for $Pd(OAc)_2$. Alcohol reduction of metal ions has been already reported by Toshima and his co-workers.[30] The reduction of $Pd(OAc)_2$ is known to proceed according to

$$Pd(OAc)_2 + CH_3OH \rightarrow Pd(0) + HCHO + 2CH_3COOH \quad (1)$$

as a spontaneous chemical reaction predictable from the electrochemical potential with respect to reduction of Pd(II) and oxidation of methanol. We should emphasize that, in this system, no specific reducing agents such as sodium borohydride ($NaBH_4$) were introduced, and the weakly reducing power of methanol was utilized to slowly reduce $Pd(OAc)_2$. Initially solution A was transparent with a dark red color and solution B was transparent and colorless. Immediately after the two solutions were mixed, the solution became slightly yellow and slightly turbid, implying rapid formation of dendrimer associations as will be clarified later. With increasing reaction time, the solution turned gradually brownish and more turbid, indicating formation of Pd nanoparticles.

2.3. UV−vis Spectroscopy. To confirm the formation of Pd nanoparticles and also to investigate local interactions between $Pd(OAc)_2$ and G1-NH_2 in the reaction medium during the reduction process, UV−vis spectroscopy was measured. The UV−vis spectra will provide us information on the coordination state of $Pd(OAc)_2$ with G1-NH_2, such as the coordination number and coordination structures.

2.4. WAXD Measurement. A wide-angle X-ray diffraction (WAXD) measurement was also performed, to confirm the formation of Pd nanoparticles. Because of the low average concentration of Pd nanoparticles, as will be discussed later in section 5.4, we could not obtain WAXD profiles of sufficient diffraction intensity for the colloidal solutions to judge whether Pd nanoparticles were formed or not. Therefore, the solution obtained at 24 h after onset of the reduction was solidified into black solid products for the WAXD measurement by evaporating the solvents. Details of the WAXD apparatus have been described elsewhere.[31,32] The WAXD profile was corrected for background (empty cell) and transmission.

2.5. Time-Resolved SANS Measurement. A detailed procedure for time-resolved SANS measurement is schematically summarized in Figure 2. After the two solutions were mixed, the reaction solution was transferred into a quartz cell with a thickness of 2 mm, followed by a time-resolved SANS measurement within less than 90 s. During the time-resolved SANS measurement, the reaction solution in the cell was placed in a temperature enclosure controlled at 50 °C with an accuracy of ± 0.5 °C. We measured SANS with a SANS-J spectrometer at the Japan Research Reactor (JRR-3) of the JAEA (Japan Atomic Energy Agency), Tokai, Japan. The incident neutron beam was monochromatized to have an average wavelength λ of 0.65 nm with a distribution of $\Delta\lambda/\lambda = 12\%$. The scattered neutrons were detected by a two-dimensional ^{3}He position sensitive detector that was 0.58 m in diameter. The obtained two-dimensional scattering patterns were radially averaged to obtain scattered intensity profiles as a function of q, where q is a magnitude of the scattering vector, defined by

$$q = \frac{4\pi}{\lambda}\sin\left(\frac{\theta}{2}\right) \quad (2)$$

with θ being the scattering angle. The SANS covered a q range of $3 \times 10^{-2} < q < 2$ nm^{-1}. The obtained scattered intensity profiles were corrected for background scattering, electronic noise of detector, detector sensitivity, and transmission of the solution and finally normalized with a porous aluminum plate, which serves as a secondary standard, to obtain the differential scattering cross-section $d\Sigma(q)/d\Omega$ in the absolute intensity scale (cm^{-1}). The scattered intensity $d\Sigma(q)/d\Omega$ was measured as a function of time t over a time period between $t - \Delta t$ and t after onset of the reduction reaction, where Δt was set to be 1 h unless otherwise stated. The scattered intensity at a given reaction time t, $d\Sigma(q;t)/d\Omega$, is evaluated by an average over the period of Δt. The exactly same procedure is applied to the acquisition of the SAXS intensity data also.

2.6. Time-Resolved SAXS Measurement. The reaction solution for SAXS was placed in a sample cell with a Teflon spacer having a thickness of 3 mm, both sides of which were sealed by Kapton films. The SAXS was measured with an apparatus which consists of an 18 kW rotating-anode X-ray generator (Bruker AXS K. K., Yokohama, Japan), and a one-dimensional position-sensitive proportional counter (PSPC). The SAXS profiles were obtained with a camera length of 1200 mm to cover the q range of $0.2 < q < 2$ nm^{-1}. The wavelength of the incident X-ray was 0.154 nm (Cu Kα line monochromatized with a graphite crystal). The obtained SAXS profiles were corrected for background scattering and slit-height and slit-width smearings. The absolute SAXS intensity was obtained by the standard nickel foil method,[33] although the absolute intensity itself is not of primary importance in this study.

2.7. Combined SANS and SAXS Method. We should note that the scattering contrast for a given system is generally different for the SANS and SAXS methods. Thus, the superpostion of the SANS and SAXS profiles in the combined SAS method can be obtained only after normalizing the $d\Sigma/d\Omega$ values for both SANS and SAXS in the absolute intensity scale by the corresponding scattering contrast, $(\Delta\rho)^2_{SANS}$ and $(\Delta\rho)^2_{SAXS}$. In the actual experiments, $d\Sigma/d\Omega$ vs q for SANS in the double-logarithmic scale is shifted vertically from that for SAXS in order to obtain the combined SAS profile in the absolute unit of the SAXS. It is important to note that parts of the SANS and SAXS profiles had a sufficiently wide q range where they superpose each other in order to ensure accuracy of the vertical shift. This method for obtaining $(d\Sigma/d\Omega)_{SAXS}$ from $(d\Sigma/d\Omega)_{SANS}$ corresponds to the manipulation given by

$$\left[\frac{d\Sigma}{d\Omega}(q)\right]_{SAXS} = \frac{(\Delta\rho)^2_{SAXS}}{(\Delta\rho)^2_{SANS}}\left[\frac{d\Sigma}{d\Omega}(q)\right]_{SANS} \quad (3)$$

where $(\Delta\rho)_{SANS}$ and $(\Delta\rho)_{SAXS}$ are respectively the scattering length density and electron density.

2.8. TEM Observations. Two samples were prepared in order to investigate the time dependence of structures as observed by TEM. One was the sample obtained from the reaction solution at $t \cong 0$ (less than 10 s after mixing the two solutions). The other was the sample obtained from the solution at $t = 48$ h after the onset of reduction (or mixing the two solutions), as a representative of the samples sufficiently reacted. A drop of each solution was placed on a copper grid, and the solvent was gradually evaporated under atmospheric pressure at room temperature. Because metal nanoparticles themselves have sufficient contrast against their matrix, we did not have to conduct specific staining prior to TEM observations. TEM observations were performed with a JEOL JEM-2000FX instrument at an accelerated voltage of 120 kV.

3. Results

3.1. UV−vis Spectroscopy. Figure 3a shows the time change in the UV−vis spectrum during the reduction process in solution.

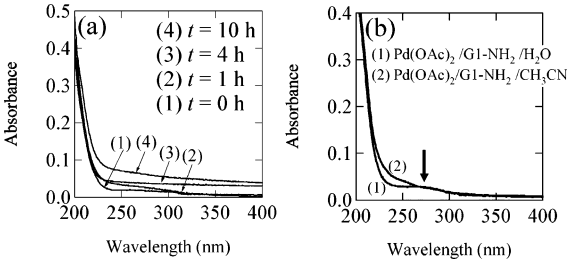

Figure 3. (a) Time evolution of the UV−vis spectrum during the reduction process. (b) Effect of solvent on the UV−vis spectrum for the mixture of $Pd(OAc)_2$ and G1-NH_2.

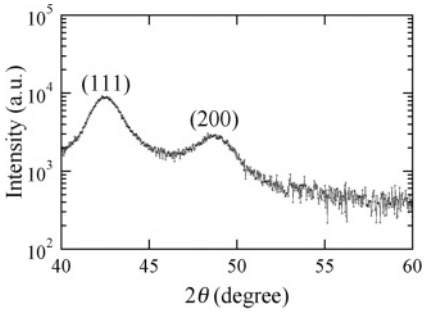

Figure 4. WAXD profile for the powders of Pd nanoparticles.

We can find a continuous increase in absorbance at the higher wavelength region of $\lambda > 250$ nm. At the lower wavelength region of $\lambda < 250$ nm, on the other hand, we can find an upturn of the absorbance with decreasing λ. However, we cannot detect a clear absorption maximum due to the complex formation between Pd(II) ions and amine groups of the dendrimer, which is of the type as shown in spectrum 1 in Figure 3b. Figure 3b shows the corresponding spectra for $Pd(OAc)_2$ and G1-NH_2 in H_2O (spectrum 1) and in CH_3CN (spectrum 2) for reference. Note that the both systems are free from reduction. Spectrum 1 in Figure 3b for the aqueous solution clearly shows a peak at 265 nm, corresponding to a ligand to metal charge-transfer band associated with complexation of Pd(II) to the amine groups of the dendrimers. The ligand to metal charge-transfer band of the palladium(II) complex with *N*,*N*′-bis(2-aminoethyl)-1,3-propanediamine was reported to appear at 284 nm in aqueous solution.[34] The maximum is less obvious in spectrum 2, obtained for a nonaqueous medium. Thus, we conclude that the complex may not be formed in the nonaqueous medium employed in this study. This conclusion is supported by a previous report claiming that salts of the transition metals Pd(II) and Cu(II) do not complex with functional groups of poly(propylene imine) (PPI) dendrimers in nonaqueous medium.[35] The metal salts are driven into PPI or PAMAM dendrimers by differential solubilities.[35,36]

3.2. WAXD Measurement. Figure 4 shows the WAXD profile for the powdered samples as obtained by the method described in section 2.4. We can find two peaks at $2\theta = 42.5$ and 48°, indicative of the diffractions from the (111) and (200) planes in a face-centered-cubic (fcc) crystal structure of Pd atoms, respectively.[37] The line width of each diffraction was found to be consistent with the size of nanoparticles as elucidated elsewhere.[38] Thus, the formation of Pd crystals was clearly confirmed. This may suggest also the fact that palladium in the nanoparticles essentially has an oxidation state of Pd(0).

3.3. Oxidation State of Palladium in the Reaction System. It may be worth noting or summarizing briefly oxidation states of palladium in both Pd nanoparticles and the dendrimer associations at this stage, although the elucidation of the state is not a main theme of this work and we have only qualitative information about it. As already described in section 2.2, immediately after mixing the two solutions A and B, the dendrimer associations are formed, which is followed by a slow reduction of $Pd(OAc)_2$ and formation of Pd nanoparticles. The results of UV−vis spectroscopy (see section 3.1) revealed no clear evidence for the ligand to metal charge-transfer complexation of Pd(II) ions to the amine groups of G1-NH_2 throughout the self-assembling process as described above. This suggests that most of the $Pd(OAc)_2$ molecules do not fully dissociate into Pd(II) ions and OAc^- ions; rather, they exist as acetate salts and associate with functional groups of G1-NH_2 if they were not reduced, throughout the self-assembling process.

The results of WAXD measurements at the end of the reduction (see section 3.2) indicated that the palladium in the nanoparticles essentially has an oxidation state of Pd(0). In a separate experiment we found that an amount of $Pd(OAc)_2$ up to 1.6 times that of the peripheral amine groups in the dendrimer is dissolved in the reaction system without reduction. The reaction system turned black beyond this concentration of $Pd(OAc)_2$. This indicates that a fraction of $Pd(OAc)_2$ is not subjected to reduction but rather acts as binders between the amine groups or strongly associated with the amine groups, the rest of the fraction is subjected to reduction. This result together with the results from UV−vis spectroscopy and WAXD may indicate the following points concerning the oxidation state. Most of $Pd(OAc)_2$ acting as binders remain as acetate salts, while most of the reduced $Pd(OAc)_2$ molecules have an oxidation state of Pd(0) in the Pd nanoparticles.

3.4. Time-Resolved SANS and SAXS Measurements. 3.4.1. Measured Profiles for SANS and SAXS. Parts a and b of Figure 5 show the time-resolved SANS and SAXS profiles at several representative reaction times, respectively. In Figure 5a, we can observe SANS scattering intensity, in excess of the average intensity from a homogeneous solution to be defined immediately below (designated as "homog. soln." and labeled by + symbols in the figure) at the lower q region of $q < 0.2$ nm^{-1} throughout the reaction process. The average intensity was defined here as the weighted average of the intensity from the homogeneous solution A and that from the homogeneous solution B. Here the relative weight was determined on the basis of the volume ratio of each solution upon mixing (0.35 mL/3.5 mL, as indicated in Scheme 1). The average intensity was accurately obtained only in the high q region of $q \geq 0.13$ nm^{-1} and found to be independent of q. The broken line represents the average intensity extrapolated to the q region of $q < 0.13$ nm^{-1}. The excess scattering at $q \leq 0.2$ nm^{-1} was already observed in the profile measured in the period between 0 and 5 min after mixing the homogeneous solutions A and B, but it exhibited almost no time dependence after 5 min, reflecting evolution of stable structures of more than 30 nm ($\cong 2\pi/q_u$ with $q_u \cong 0.2$ nm^{-1}) in the characteristic length scale (designated hereafter "large domain" or "domain template") formed in the reaction medium on a time scale of less than ~5 min. The estimated average scattering intensity is considered to be mainly caused by incoherent scattering of the reaction system.

One might suspect that the trend that the SANS from the domain template does not change with time in the time scale covered in this experiment implies that the SANS reflects some impurities present in the system rather than the domain templates themselves. However, this suspicion is clearly removed by the following pieces of evidence. (1) Solutions A and B before mixing are clear homogeneous solutions which give rise to no

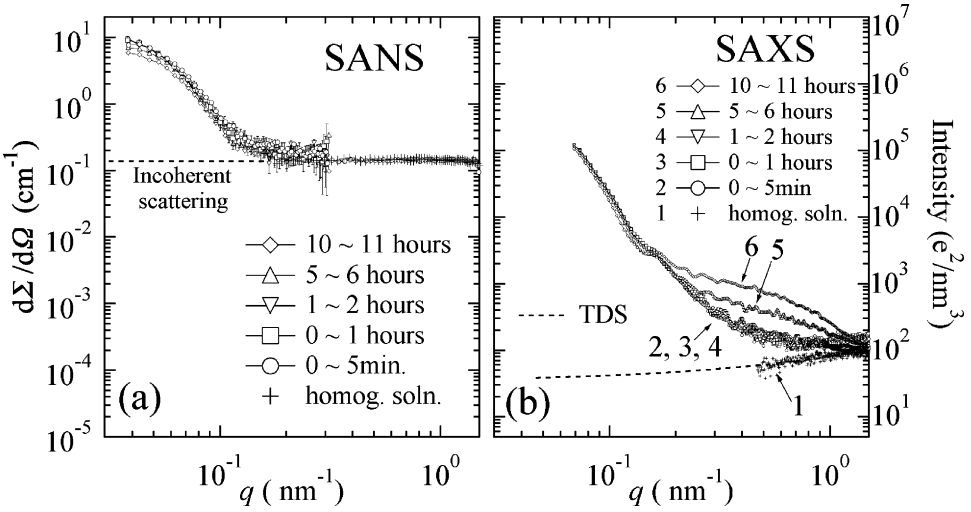

Figure 5. Time evolution of (a) SANS profiles and (b) SAXS profiles after mixing the two solutions as well as SANS and SAXS profiles for the average scattering intensity from the homogeneous solution (see details in the text).

excess scattering beyond the incoherent scattering level; translucence of the mixed solution appears quickly only after mixing the two solutions, indicating that the template will be formed quickly after the mixing. (2) At a given concentration of $Pd(OAc)_2$, $[Pd(OAc)_2] = 3.6$ mM, and with a fixed ratio r of $[Pd(OAc)_2]$ and concentration of total terminal amine groups of dendrimers $[-NH_2]$, $r = [Pd(OAc)_2]/[-NH_2] = 3.33$, we found that the size of the template systematically decreases with increasing generation number from 1 to 3, as will be detailed in a paper to follow,[39] although in all of the cases the template formation quickly occurs less than 5 min after mixing. (3) At a fixed concentration of $Pd(OAc)_2$ ($[Pd(OAc)_2] = 3.6$ mM) and for G1-NH_2, we found that there is a critical concentration of $[-NH_2]$, above which the templates cannot be formed and the dendrimers are isolated in the solution, as will be also detailed in a later paper.[39] (4) Similar template domains were also observed by Naka et al.[26,38]

Figure 5b shows the time change in the SAXS profiles. The SAXS profile for the estimated average scattered intensity from the two homogeneous solution A and B (profile 1, defined as "homog. soln." in the figure legend) is also shown by the symbol (+) in the q region of $q \geq 0.5$ nm^{-1}. In the lower q region of $q < 1.5$ nm^{-1}, the SAXS scattered intensity in excess of the average intensity is always detectable throughout the reaction process. The excess scattering in the low q region of $q < 0.15$ nm^{-1} shows almost no time change, as in the excess SANS scattering observed in the same low q region. In contrast, in the higher q region of $q > 0.2$ nm^{-1}, we can find a steady increase of the SAXS excess scattered intensity with increasing reaction time. The increase in the scattered intensity is expected to originate from creation of the Pd nanoparticles in the reaction solution, as will be detailed later. The increase in the average scattered intensity toward higher q is due to thermal diffuse scattering (TDS) arising from the homogeneous solution. The TDS intensity level can be estimated by the following semiempirical relationship proposed by Vonk,[40] as shown by a broken line:

$$I_{TDS}(q) = a + bq^n \tag{4}$$

where a, b, and n indicate constant values.

3.4.2. Correction of the SAXS and SANS Profiles and Construction of the Combined SAS Profile. For further analysis of the scattering profiles, we have to first subtract the incoherent scattering and the TDS, both of which essentially correspond to the average intensity of the two homogeneous solutions, from a series of the observed time-resolved SANS and SAXS profiles, respectively, as will be detailed elsewhere.[41] The two corrected SAS (SANS plus SAXS) profiles at a given time after the mixing of the two solutions were smoothly superposed on each other by a vertical shift of the SANS profile relative to the SAXS profile to construct the combined SAS profile, as detailed in section 2.7 and ref 41. An appropriately wide overlapping q region of $0.1 < q < 0.2$ nm^{-1} in the SANS and SAXS profiles enables us to accurately obtain the combined profile.

3.4.3. Time-Resolved Combined SAS Profiles. Figure 6a presents the time evolution of the combined SAS profiles in the absolute intensity scale of SANS during the reaction process, which are constructed according to the method as described above. In the figure, we present only five profiles at representative reaction times for clarity (to avoid overlapping). In Figure 6b is shown the time change in the scattered intensity at the two representative q values of 0.04 and 0.6 nm^{-1}, as indicated by the arrows in Figure 6a, during the whole reaction process. Figure 6b contains all data points measured in this time-resolved study, in addition to the data plotted Figure 6a. From the time change in the scattered intensity, we can find that the scattered intensity at the low q value of $q = 0.04$ nm^{-1} is nearly constant with time, though a slight decrease can be recognized. In contrast, the scattered intensity at the high q value of $q = 0.6$ nm^{-1} increases by more than 10 times when the reaction time is increased.

3.5. TEM Observations. Parts a and b of Figure 7 present typical TEM images observed at $t = 10$ s and 48 h after onset of the reaction, respectively. In Figure 7a, we can see dark large spherical domains with an average diameter of 60−70 nm. Some of them seem to be interconnected with each other, which is believed to be artifacts resulting from a structural change in the solvent evaporation process to prepare the film specimens for the TEM observation. However, the large spherical domains are believed to be free from artifacts developed during the solvent evaporation process. One might suspect that the domains observed by TEM arise from the fast evaporation of methanol and slower evaporation of DMF. However, since DMF itself is a good solvent for both dendrimers and $Pd(OAc)_2$, this suspicion is ruled out. Moreover, the solution obtained by mixing the two homogeneous transparent solutions A and B became translucent

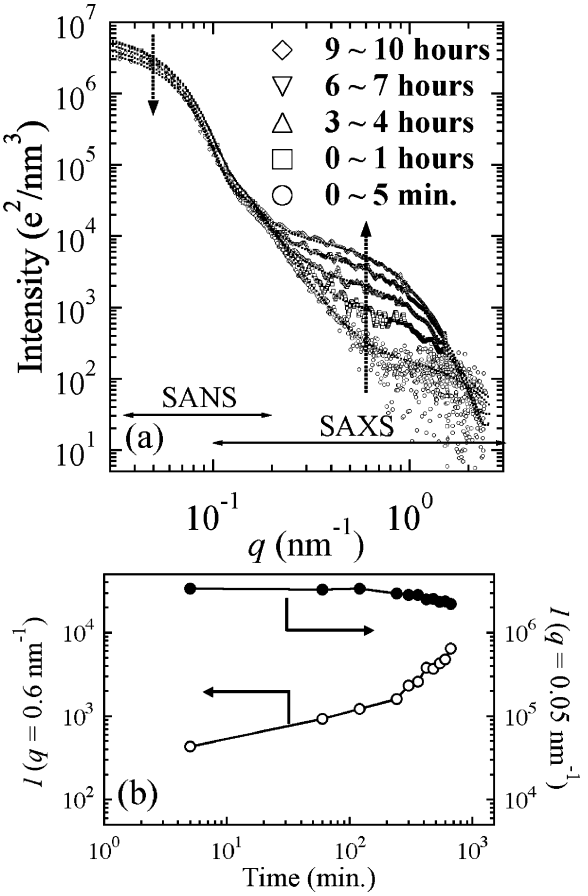

Figure 6. (a) Time evolution of combined SAS (SANS plus SAXS) profiles during the reduction process. (b) Time change in the scattered intensity at $q = 0.05$ and 0.6 nm^{-1}.

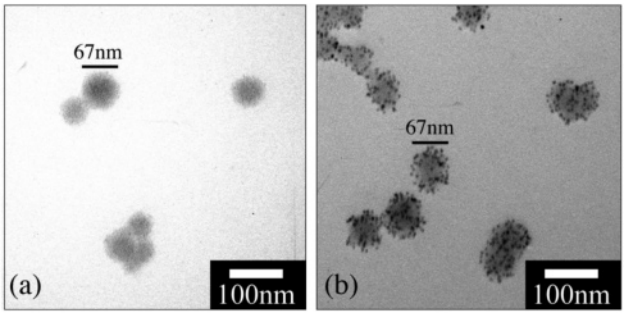

Figure 7. Typical TEM images obtained from solution (a) just after mixing (less than 10 s) of solutions A and B (b) 48 h after mixing.

soon after mixing, indicating the existence of large domains in the solution even before solvent evaporation. At any rate, it is crucial to explore in situ the structures existing in the solution by means of SANS and SAXS. This point will be discussed in section 5.

Figure 7b shows a typical TEM image at $t = 48$ h, where numbers of small particles with average diameters of several nanometers (nanoparticles) are confirmed to exist within the large spherical domains as found in Figure 7a. Moreover, it is found that almost all nanoparticles are trapped inside the spherical domains. The spherical domains seem to serve as a template which entraps and stabilizes the nanoparticles. It is also noted that, with increasing reaction time, the size of the templates does not change but is rather kept almost constant, though the relevant TEM's as a function of reaction time are not shown here. Again, we can notice some of the domains

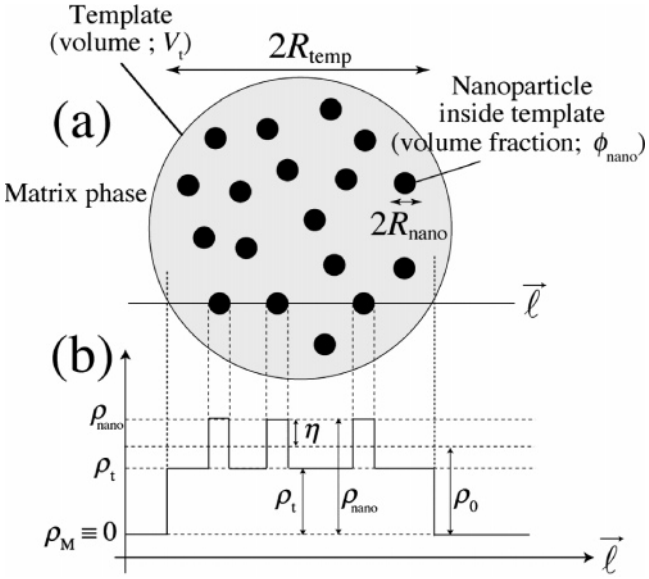

Figure 8. (a) Schematic illustration of a spherical template of radius R_{temp} having an assembly of nanoparticles as an internal structure. (b) Scattering contrast profile across the template.

containing nanoparticles being interconnected to each other, although it has not been clearly judged whether the domains are isolated from each other or are interconnected in the actual reaction solution by the TEM images alone for the same reason described above. This point should be best analyzed in situ in the solution by the scattering method proposed in this paper.

4. Scattering Theory

4.1. The Scattering Function Appropriate for the System of Interest. We aim to analyze scattering profiles from such a specific structure having a complicated hierarchical structure, as shown in Figure 7b. In order to properly analyze the scattering profiles, we assume a simplified model as depicted in Figure 8a, which schematically illustrates an assembly of nanoparticles in a template. The average radii of the nanoparticles and the template are denoted as R_{nano} and R_{temp}, respectively. The template is an aggregate of palladium acetate and G1-NH_2 swollen with solvent and is dispersed in the matrix of solvent. Figure 8b indicates the scattering contrast profile across the assembly along the vector **l** in Figure 8a.

On the basis of the well-established small-angle scattering theory,[42−44] we derived the theoretical scattering function $I_{exact}(q)$ applicable to our system, which comprises isolated templates giving rise to independent scattering. The validity of the assumption concerning the independent scattering will be given in section 5.4. The scattering function per single template, $I_{exact}(q)$, is given by[41]

$$I_{exact}(q) = V_t{\rho_0}^2\left[S_{temp}(q) + \frac{\langle\eta^2\rangle}{{\rho_0}^2}S_{temp}(q) * S_{nano}(q)\right] \quad (5)$$

where $S_{temp}(q)$ and $S_{nano}(q)$ indicate scattering functions for the templates and the nanoparticles, and the symbol * denotes the convolution product of the two scattering funcitons. In the case when $R_{temp} \gg R_{nano}$, $S_{temp}(q)$ can be approximated by the delta function, so that $I_{excat}(q)$ is given by an approximated function, $I_{approx}(q)$, as detailed also in ref 41:

$$I_{approx}(q) = V_t{\rho_0}^2\left[S_{temp}(q) + \frac{\langle\eta^2\rangle}{{\rho_0}^2}S_{nano}(q)\right] \quad (6)$$

In eqs 5 and 6, V_t and ρ_0 denote the volume of the template and an average scattering contrast for the template containing nanoparticles, respectively. The latter is given by

$$\rho_0 = \phi_{nano}\rho_{nano} + (1 - \phi_{nano})\rho_t \tag{7}$$

where ϕ_{nano}, ρ_{nano}, and ρ_t denote the volume fraction of nanoparticles in the template and the scattering contrast of the nanoparticle and that of the template, respectively. The volume fraction ϕ_{nano} is given by

$$\phi_{nano} = N_{nano}(R_{nano}/R_{temp})^3 \tag{8}$$

where N_{nano} denotes the total number of nanoparticles in the template. In eqs 5 and 6, $\langle\eta^2\rangle$ denotes the mean-square fluctuations for the spatial variation of scattering contrast in the template as shown in Figure 8b. Thus, $\langle\eta^2\rangle/\rho_0^2$ is given by

$$\frac{\langle\eta^2\rangle}{\rho_0^2} = \frac{(\rho_{nano} - \rho_t)^2}{\rho_0^2}\phi_{nano}(1 - \phi_{nano}) \tag{9}$$

The approximation used in eq 6 will be justified only when $R_{temp} \gg R_{nano}$ is satisfied, as clarified later. It is worth noting that in this case small-angle scattering from the complicated structure as depicted in Figure 8a can be expressed by a weighted sum of two scattering functions: (i) the scattering function for templates $S_{temp}(q)$ and (ii) that for nanoparticles $S_{nano}(q)$.

One should note that only the terms ρ_0^2 and $\langle\eta^2\rangle/\rho_0^2$ depend on incident beam source: X-ray or neutron. This factor should be correctly taken into account when the combined SAS scattering curve is constructed, as already pointed out in section 2.7.

4.2. Scattering Function for Nanoparticles and Templates. Let us consider $S_{temp}(q)$ and $S_{nano}(q)$ in eqs 5 and 6. We can assume that both nanoparticles and templates have a spherical shape, judging from the TEM images in Figure 7a,b. Hence, the two scattering functions $S_{temp}(q)$ and $S_{nano}(q)$ can be written as

$$S_J(q) = CN_J\int_0^\infty \left[\frac{4\pi R^3}{3}\right]^2 [\Phi(qR)]^2 P_J(R)\, dR \tag{10}$$

where

$$\Phi(qR) = \frac{3}{(qR)^3}[\sin(qR) - (qR)\cos(qR)] \tag{11}$$

and the suffix J refers to the suffix nano or temp. N_{temp} is the total number of templates, $P_{nano}(R)$ and $P_{temp}(R)$ are normalized distribution functions, which give respectively the number of nanoparticles and templates having a radius of R, and C is the proportionality constant independent of q, associated partially with the scattering contrast. It should be noted that in eq 10 we implicitly assume both nanoparticles and templates have no spatial correlation with each other: i.e., the scattering intensity from nanoparticles (or templates) can be expressed by a sum of the scattering intensity from isolated nanoparticles (or templates). The legitimacy of this assumption will be discussed in section 5.4. In eq 10 we assume that both $P_{nano}(R)$ and $P_{temp}(R)$ have a Gaussian distribution defined by

$$P_J(R) = \frac{1}{\sqrt{2\pi}\sigma_J}\exp\left[-\frac{(R - R_J)^2}{2\sigma_J^2}\right] \tag{12}$$

$$\int_0^\infty P_J(R)\, dR = 1$$

where J is the suffix nano or temp, R_{nano} and R_{temp} are respectively the number-averaged radii of nanoparticles and templates, and σ_{nano} and σ_{temp} are standard deviations of the size of nanoparticles and templates from the average values, respectively.

4.3. Numerical Analysis for Validity of the Approximated Scattering Function $I_{approx}(q)$. We examined the validity of the approximated equation (6) by numerical calculations and by comparisons of $I_{exact}(q)$ and $I_{approx}(q)$ for five different values of $r_R \equiv R_{temp}/R_{nano}$ under the conditions where other parameters are fixed, as detailed elsewhere.[41] The results confirmed that $I_{approx}(q)$ given by eq 6 is valid in the case of $r_R \equiv R_{temp}/R_{nano} \geq 15$. This criterion is well satisfied in this study because the average radii of the templates and the Pd nanoparticles are estimated to be 30 and ca. 2 nm, respectively, from the TEM image in Figure 7b. Therefore, we can employ the approximated equation (6) for further quantitative analysis of the series of time-resolved scattering profiles, as given by Figure 9.

5. Discussion

5.1. Time Evolution of Hierarchical Structures. In order to investigate quantitatively the time evolution of both the templates and the Pd nanoparticles, we further analyzed the experimental scattering profiles by using the theoretical scattering function given by eq 8. In Figure 6a, the dotted lines show the predicted scattering profiles best-fitted with the experimental profiles. It is found that the observed scattering profiles can be well reproduced by the approximated function (eq 8), implying that the templates are spherical and are isolated from one another. Thus, the interconnection of the templates observed in the TEM images in Figure 7 may be brought about during the solvent evaporation of the solution on the microscope grids.

In order to highlight the characteristics of each scattering profile and the accuracy of the best-fitted scattering profiles more clearly than Figure 6a, we present Figure 9, where each profile was vertically shifted to avoid an overlap. The scattering profile obtained from 0 to 5 min after mixing the two solutions tends to exhibit the asymptotic behavior of q^{-4} at $0.1 \leq q \leq 0.5$ nm^{-1} (Porod's law), indicating the scattering from templates with a smooth surface and a sharp boundary normal to the surface.[45] The profile tends to exhibit an upward deviation from Porod's law at $q \geq 0.5$ nm^{-1}, which is elucidated to arise from $S_{nano}(q)$: the formation of nanoparticles inside the template gives rise to the excess scattering to the scattering from a homogeneous template $S_{temp}(q)$ in the high q range. With increasing reaction time, the excess scattering from $S_{nano}(q)$ increases, so that Porod's law can be discerned in a narrower q range, because the upper bound of q for Porod's law decreases. Porod's law finally becomes invisible for the profiles obtained later than 6 h after the mixing. Instead, we can find another Porod's law behavior in a much higher q range of $q > 1.0$ nm^{-1}, which is due to the asymptotic behavior of $S_{nano}(q)$ arising from the nanoparticles. The broad maximum labeled by the arrow is found to arise from the form factor of the template.

The best fit yielded information on time changes in both R_{temp} and R_{nano} during the reaction process. The time evolutions of

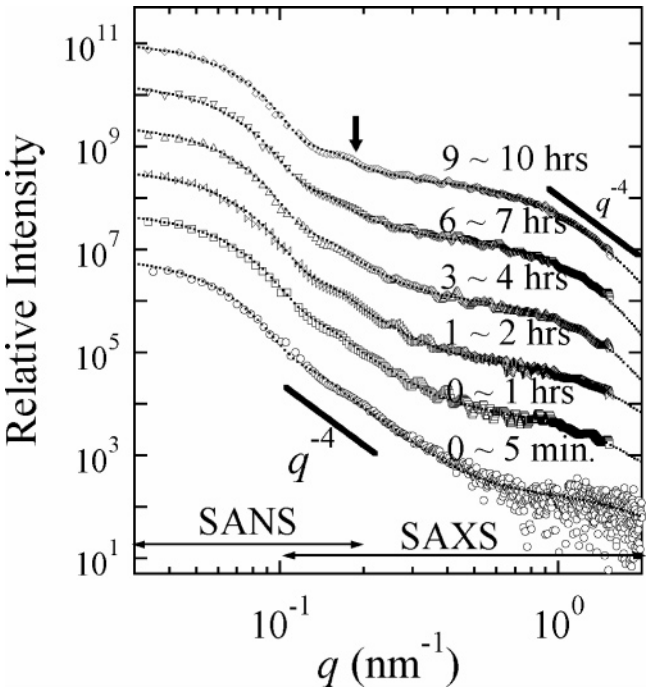

Figure 9. Theoretical scattering profiles calculated from eq 8 (shown by dotted lines) best-fitted with the experimentally obtained SAS profiles (shown by symbols). The profiles are vertically shifted to avoid their overlaps in order to highlight detailed features of each profile and to clarify the state of the best fits.

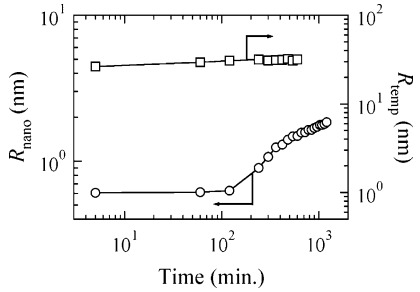

Figure 10. Time evolution of average radius of palladium nanoparticles R_{nano} and template R_{temp}.

R_{temp} and R_{nano} thus estimated are presented in Figure 10. Surprisingly enough, at all time regions covered in this study ($5 < t < 660$ min), R_{temp} shows an almost constant value of 30 nm, quite consistent with the size observed in the TEM images in Figure 7a,b. It is important to note here that the evaluated size of the templates R_{temp} is larger than that of one dendrimer molecule by a factor of 40, because the radius of gyration of G1-NH_2 (R_g) is theoretically calculated to be 0.75 nm.[46] This suggests that the template structures observed in this study are composed of many dendrimers and $Pd(OAc)_2$ as binders for the interdendrimer association, which is a situation totally different from that encountered in most of the previous relevant studies.[16−25]

As for the time change in R_{nano}, it increases from 0.6 to 2.0 nm with the reaction time. Although r_R decreases from 50 to 15 with the time, the range of r_R still ensures the validity of using $I_{approx}(q)$ in eq 8 for the scattering analysis. It is also noteworthy that at the early stage of $0 < t < 120$ min, R_{nano} shows an almost constant value of ca. 0.6 nm, and only after $t = 120$ min a gradual increase of its value becomes obvious: a rapid increase first ($R_{nano} \approx t^{1/2}$ for $120 < t < 520$ min), followed by a slow increase ($R_{nano} \approx t^{1/3}$ for $t > 520$ min). It should be stressed that the value R_{nano} can be larger than the value R_g for G1-NH_2. This would not occur in the earlier studies,[16−27] which dealt with the case of single dendrimers acting as templates: i.e., the case of reduction of metal ions encapsulated in an isolated single dendrimer and formation of metal particles in the same dendrimer. In this case we expect that R_{nano} is smaller than R_g. In our case, however, metal particles formed in one dendrimer can interact with those formed in another dendrimer within the dendrimer aggregate as a template, so that R_{nano} can be larger than R_g. It is intriguing to note that the slowdown in the growth of R_{nano} at $t > 520$ min corresponds to the case where R_{nano} becomes larger than $2R_g$.

The time period of $0 < t < 120$ min appears to correspond to the incubation period for the growth of R_{nano}, and after this period, an accelerated growth of R_{nano} will take place. Interpretations of this intriguing behavior deserve future sutdy. It may be worth noting that even in the early stages the scattered intensity $I(q = 0.6\ nm^{-1})$ from the nanoparticles increases with time, as evidenced by Figure 6b (open circles). This may imply that the number of Pd nanoparticles may increase with time in the early stages. It should again be emphasized that the size of the templates is hardly affected by the growth of Pd nanoparticles. Thus, we can demonstrate that the formation of the templates is almost completed within 5 min after the mixing of the two solutions and beginning of the reaction, and the reduction of $Pd(OAc)_2$ and the resulting formation of Pd nanoparticles proceed rather slowly within the templates of the dendrimer associations. The relative standard deviation for the template size σ_{temp}/R_{temp} remains constant with time at 0.2, but that for the nanoparticle size σ_{nano}/R_{nano} decreased from 0.65 to 0.5 with time.

5.2. Self-Assembling Process. The observed time changes in R_{temp} and R_{nano} will enable us to visualize the self-assembling process of the dendrimer templates and Pd nanoparticles, as summarized in parts a−d of Figure 11: Figure 11a schematically illustrates a homogeneous solution of $Pd(OAc)_2$ and G1-NH_2 in the solvent composed of DMF and methanol, where $Pd(OAc)_2$ and G1-NH_2 are denoted by dots and crosses, respectively. The schematic illustration approximately takes into account the relative number and size of $Pd(OAc)_2$ and G1-NH_2 as follows. $Pd(OAc)_2$, having a characteristic size of approximately 0.16 nm, is much smaller than G1-NH_2, having a characteristic size ($2R_g$) of approximately 1.5 nm, by about a factor of 10. Since G1-NH_2 has eight primary amine groups and $r = [Pd(OAc)_2]/[-NH_2] = 3.3$ as shown in Table 1, $[Pd(OAc)_2]/[G1\text{-}NH_2] = r[-NH_2]/[G1\text{-}NH_2] = 3.3 \times 8 = 26.4$, so that the number of $Pd(OAc)_2$ groups is much larger than that of G1-NH_2. Figure 11b schematically illustrates the formation of spherical templates comprising self-assembled $Pd(OAc)_2$ and G1-NH_2 in the solution, prior to the reduction of $Pd(OAc)_2$. Figure 11c schematically illustrates the reduction of $Pd(OAc)_2$ within the template into Pd(0) atoms and their self-assembly into nanoparticles having an average diameter of 1.2 nm in the early stage. Figure 11d shows the further progress of the reduction reaction, which gives rise to an increased number and size of nanoparticles.

During the course of formation and growth of the Pd nanoparticles, the template structure and size are kept constant. The templates provide stable specific fields for the reduction reaction of $Pd(OAc)_2$ and for the unique self-assembly of Pd(0) atoms into Pd nanoparticles.

5.3. Mechanism of the Self-Assembly of Dendrimer Templates and Pd Nanoparticles. In this section, we wish to discuss possible mechanisms of the self-assembly of the dendrimer templates and the Pd nanoparticles. We wish to address questions on why the spherical template structures are

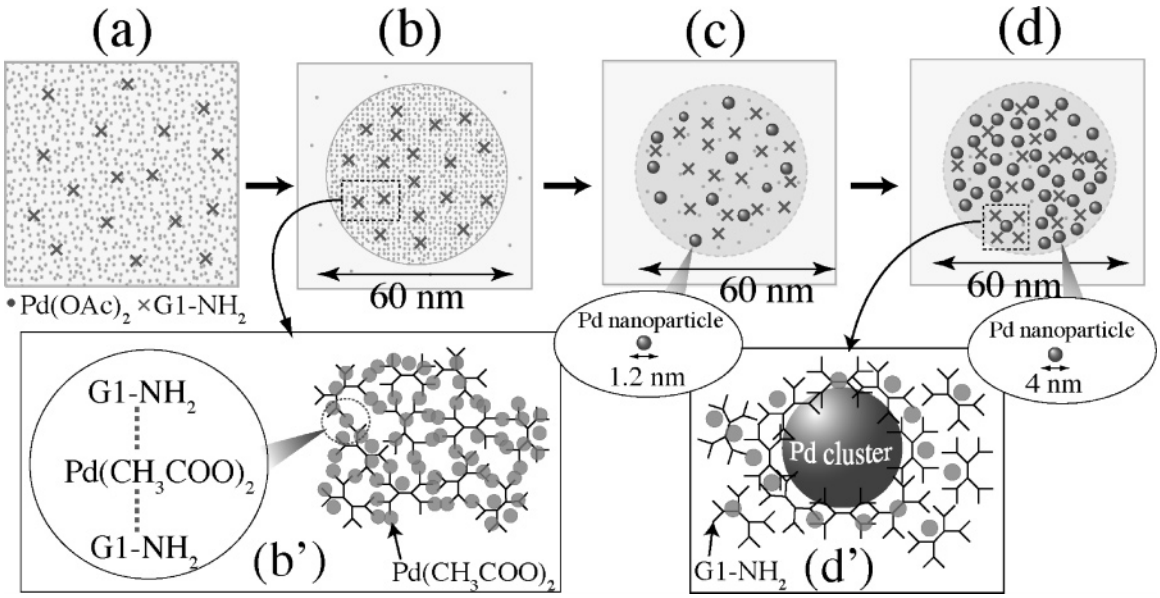

Figure 11. Summary of self-assembling processes of the dendrimer templates and Pd nanoparticles as elucidated from the combined SANS and SAXS method.

formed and what kinds of physical and/or chemical factors are crucial for controlling the templates.

First, let us consider the interactions among G1-NH_2, Pd-$(OAc)_2$, DMF, and methanol. As briefly mentioned in sections 3.1 and 3.3, the UV−vis spectra reveal that most of the Pd-$(OAc)_2$ in the reaction solution remains as acetate salts. They are expected to be solubilized in the interior space of dendrimers and are associated with the functional groups, though the association strength depends on the types of functional groups. Since the total number of the functional groups per single dendrimer is 26 and our experimental system has the stoichiometric relationship $[Pd(OAc)_2]/[G1\text{-}NH_2] = 26.4$, most of the $Pd(OAc)_2$ in the system will be solubilized in the interior space of the dendrimers and associated with the functional groups, as illustrated in Figure 11b′, which is an enlargement of Figure 11b, where the dendrimer is shown by solid lines and only some of the $Pd(OAc)_2$ are shown by gray circles. The solubilization and association of $Pd(OAc)_2$ in G1-NH_2 may occur, because attractive interactions of $Pd(OAc)_2$ with the functional groups in the dendrimer, which may be due to ion−dipole and/or dipole−dipole interactions, are stronger than the following two attractive interactions: attractive interactions between $Pd(OAc)_2$ and DMF and attractive interactions between the functional groups of the dendrimers and DMF or methanol.

This association of $Pd(OAc)_2$ with the functional groups of the dendrimer will in turn suppress the miscibility of the dendrimers with the solvents (DMF and methanol) and the miscibility of $Pd(OAc)_2$ with DMF and hence provide a thermodynamic driving force for formation of the templates comprising the dendrimers and $Pd(OAc)_2$ as shown in Figure 11b,b′. The primary amine groups in the periphery of the dendrimers have the strongest attractive interactions with Pd-$(OAc)_2$, in comparison with the other functional groups in the dendrimer. Those interactions of $Pd(OAc)_2$ with the primary amine groups which belong to different dendrimers dominantly act as cross-links between different dendrimer molecules, as schematically illustrated in the left half of Figure 11b′. The weak reducing power of methanol also should be crucial for keeping the interdendrimer cross-links, because the reduction power may not be strong enough to reduce $Pd(OAc)_2$ acting as binders. If $Pd(OAc)_2$ salts as binders are reduced, they will not act as binders and the domain templates will be broken. Thus, a fraction of $Pd(OAc)_2$ is not subjected to reduction but rather is kept to act as binders between the amine groups, and the rest of the fraction is subjected to reduction, as already pointed out in section 3.3. If the reducing power is stronger than the attractive interactions, $Pd(OAc)_2$ will be reduced so that the interdendrimer cross-links may be destroyed, as previously reported by Naka et al. in the case of using $NaBH_4$ as a strong reducing agent.[38]

Formation of the dendrimer templates is favored by energetic interactions, while it is disfavored by loss of entropy: (i) the translational entropy of the dendrimers and $Pd(OAc)_2$ and (ii) the conformational entropy of the dendrimers. The latter occurs because the interdendrimer cross-links via the interactions between the amine groups and $Pd(OAc)_2$ involves distortion of the dendrimer conformation or a loss of conformational freedom of the dendrimers. The template of the dendrimers may be formed as a consequence of the energetics outweighing the entropy. However, the template may not be grown into infinitely large objects but rather be stabilized at a certain finite size (about 60 nm in diameter under these experimental conditions). This is because, as templates become large, the effective contact area between the two templates per total surface area of the template becomes small. This reduces the effective binding force connecting two templates via attractive interactions between Pd-$(OAc)_2$ and the amine groups belonging to the different dendrimers, as illustrated in Figure 12. As a consequence, the binding force becomes relatively weaker than the random thermal force acting on templates.

$Pd(OAc)_2$ molecules which are weakly associated with the functional groups will be reduced into Pd(0) atoms. The atoms thus formed are less interactive with the templates than Pd-$(OAc)_2$ and undergo vigorous Brownian motion in the templates, which corresponds to a gaseous state for Pd atoms, and these coalesce with other atoms to form small nanoparticles having $R_{nano} = 0.6$ nm, as shown in Figure 11c, the process of which may change Pd atoms from the liquid state to the solid state.

The small nanoparticles will further grow in the medium of the templates via coalescence with other small nanoparticles or Pd(0) atoms newly reduced. However, as the particles become larger than the size of the dendrimers, Brownian motions of

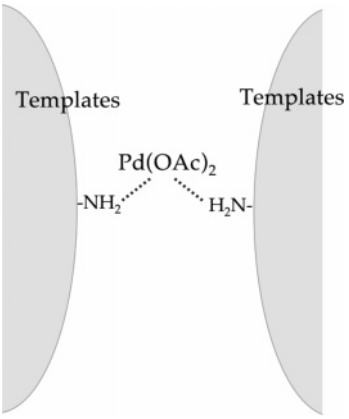

Figure 12. Schematic illustration of the origin of the binding force between the dendrimer templates.

the particles are slowed down and eventually pinned, because the translational motion causes deformation of the dendrimers and destructions of the cross-links in the templates and re-formation of the new cross-links, thus involving the costs of mechanical and thermodynamic work. Grown particles as large as $R_{nano} = 2$ nm will be therefore entrapped and stabilized in the template, as schematically shown in Figure 11d′. We should stress that the stabilization mechanism of nanoparticles in this system is quite different from that reported in the previous studies: i.e., the stabilization of metal nanoparticles via encapsulation in the interior space of single dendrimers.

In our system, templates may be deformed into anisotropic shapes and oriented upon exposing various external fields such as mechanical fields, electric fields, magnetic fields, and so on. The nanoparticles themselves also may be aligned under the external fields. Manipulations of the self-assembly based on the principle as described here may be quite useful for creating controlled, advanced materials.

5.4. Estimation of ϕ_{temp} and ϕ_{nano}. We shall evaluate the approximate volume fraction of dendrimer aggregate (template) in the solution, ϕ_{temp}, and volume fraction of Pd nanoparticles within the templates, ϕ_{nano}. From the experimental conditions of $[Pd(OAc)_2]/[G1\text{-}NH_2] = 26$ and $[Pd(OAc)_2] = 3.6$ mmol/L, we obtain $[G1\text{-}NH_2] = 3.6/26 = 0.14$ mmol/L. With this value, together with the radius of gyration for G1-NH_2 of 0.75 nm,[46] we can evaluate the total volume fraction of G1-NH_2 in the solution, ϕ_{G1}, as $\phi_{G1} = [4\pi/3 \times (0.75)^3] \times [0.14 \times 10^{-3}] \times [6.02 \times 10^{23}]/10^{24} = 1.49 \times 10^{20}/10^{24} = 0.015$ vol %, noting that 1 L $= 10^{24}$ nm^3. $\phi_{temp} \leq \phi_{G1}$, because some of the dendrimers may exist in the solution free from the large dendrimer aggregates. Thus, ϕ_{temp} is an extremely small value, and hence the dendrimer templates are expected to be well isolated from each other.

The value ϕ_{nano} can be evaluated from the mass density of Pd particles (=12.02 g/cm^3), the molecular weight of Pd (=106.4 g/mol), and $[Pd(OAc)_2]$ (=3.6 mmol/L): $\phi_{nano} = (3.6 \times 10^{-3}) \times (106.4/12.02)/(1.49 \times 10^{20}) = 0.21 = 21$ vol %. This is the maximum value obtained in the case when all Pd-$(OAc)_2$ molecules are reduced into Pd(0) atoms and aggregated into the Pd nanoparticles of $R_{nano} \geq 0.6$ nm as observed by SAXS. Since there are some $Pd(OAc)_2$ molecules which may not be reduced into Pd(0) atoms and there are Pd nanoparticles with $R_{nano} < 0.6$ nm which cannot be detected by SAXS, the effective ϕ_{nano} value for SAXS may be less than 10 vol %.

6. Concluding Remarks

We presented the self-assembly of molecules in an open-nonequilibrium system which is developed by mixing two stable solutions. In this particular work, $Pd(OAc)_2$ in DMF and G1-NH_2 dendrimer in methanol are used as the two stable solutions. The mixing of the two solutions imposes energy on the system which triggers both self-assembly and chemical reactions for some components in the system, thus giving rise to a strong interplay between the chemical reaction and the self-assembly of molecules in the system. In the particular system we studied, the unique self-assembly involves first aggregation of the dendrimers via interdendrimer cross-linking, for which $Pd(OAc)_2$ acts as a binder, and subsequently self-assembly of Pd(0) atoms as a reaction product into Pd nanoparticles. The dendrimer aggregates act as a template which provides a special field (or a specific site) for the chemical reaction involving reduction of $Pd(OAc)_2$ into Pd(0) atoms and for the self-assembly of Pd(0) atoms into Pd nanoparticles. In this case R_{nano} can exceed R_g of the single dendrimer, as pointed out in section 5.1. The nanoparticles are stabilized in the template, because their growth or agglomeration involves free energy cost arising from the elastic deformation of the dendrimers and fracture of the dendrimer network in the template. In other words, the growth of R_{nano} is unfavorable when $R_{nano} \geq 2R_g$, causing the suppressed growth rate.

7. Perspectives

In addition to clarification of the self-assembling process and the mechanism of the dissipative structures as described above, this work may also elucidate a new method for stabilizing nanoparticles trapped in the dendrimer aggregates (templates) in contrast with the traditional method, which involves stabilization of a single nanoparticle trapped and stabilized by a single dendrimer. The metal nanoparticles trapped in the dendrimer templates will give perspectives for further alignments of the templates and nanoparticles under external fields such as shear flow field and electric field. The manipulation of the dissipative structures under the external fields may be conducted during and/or after the self-assembling processes. The template formation would be quite useful for such manipulation as described above.

This unique self-assembly was brought about primarily by (i) strong attractive interactions between G1-NH_2 and $Pd(OAc)_2$ in the reaction medium, (ii) a large value of $r = [Pd(OAc)_2]/[-NH_2]$, and (iii) a weak reducing power of methanol for Pd-$(OAc)_2$ associated with G1-NH_2. These pieces of information would be useful for sophisticated controls of the templates and nanoparticles. For example, as a consequence of the present studies, we can expect that changing the parameter r will give the following effects: increasing r above a critical value will result in precipitation of unstabilized large Pd particles; decreasing r by the way of increasing $[-NH_2]$ via increasing GN under a constant $[Pd(OAc)_2]$ will decrease R_{temp} but increase R_{nano}; decreasing r below a critical value will result in formation of isolated dendrimers encapsulating a single Pd nanoparticle. A systematic study of these effects of GN and r on R_{temp} and R_{nano} will be reported in a later paper.[39] The combined SAS method was demonstrated to be quite useful for the self-assembly of mesoscopic-scale structure in open nonequilibrium systems.

Acknowledgment. We gratefully acknowledge financial support by the 21st Century COE Program for a United Approach to New-Materials Science.

References and Notes

(1) Schmidt, G. *Clusters and Colloids from Theory to Application*; VCH: Weinheim, Germany, 1992.

(2) Simons, U.; Schön, G.; Schmidt, G. *Angew. Chem., Int. Ed. Engl.* **1993**, *32*, 250−254.
(3) Andres, R. P.; Bielefeld, J. D.; Henderson, J. I.; Janes, D. B.; Kolagunta, V. R.; Kubiak, C. P.; Mahoney, W. J.; Osifchin, R. G. *Science* **1996**, *273*, 1690−1693.
(4) El-Sayed, M. A. *Acc. Chem. Res.* **2001**, *34*, 257−264.
(5) Kubo, R. *J. Phys. Soc. Jpn.* **1962**, *17*, 975−986.
(6) Kawabata, A. *J. Phys. Soc. Jpn.* **1970**, *29*, 902−911.
(7) Ng Cheong, C. Y.; Craig, G. S. W.; Schrock, R. R.; Cohen, R. E. *Chem. Mater.* **1992**, *4*, 885−894.
(8) Antonietti, M.; Förster, S.; Hartmann, J.; Östereich, S. *Macromolecules* **1996**, *29*, 3800−3806.
(9) Seregina, M. V.; Bronstein, L. M.; Platonova, O. A.; Chernyshov, D. M.; Valetsky, P. M. *Chem. Mater.* **1997**, *9*, 923−931.
(10) Klingelhöfer, S.; Heitz, W.; Greiner, A.; Östereich, S.; Förster, M.; Antonietti, M. *J. Am. Chem. Soc.* **1997**, *119*, 10116−10120.
(11) Hashimoto, T.; Saijo, K.; Harada, M.; Toshima, N. *J. Chem. Phys.* **1998**, *109*, 5627−5638.
(12) Tsutsumi, K.; Funaki, Y.; Hirokawa, Y.; Hashimoto, T. *Langmuir* **1999**, *15*, 5200−5203.
(13) Sakamoto, N.; Harada, M.; Hashimoto, T. *Macromolecules* **2006**, *39*, 1116−1124.
(14) Reetz, M. T.; Westermann, E. *Angew. Chem., Int. Ed.* **2000**, *39*, 165−168.
(15) Deshmukh, R. R.; Rajagopal, R.; Srinivaan, K. V. *Chem. Commun.* **2001**, 1544−1545.
(16) Zhao, M.; Sun, L.; Crooks, R. M. *J. Am. Chem. Soc.* **1998**, *120*, 4877−4878.
(17) Balogh, L.; Tomalia, D. A. *J. Am. Chem. Soc.* **1998**, *120*, 7355−7356.
(18) Esumi, K.; Suzuki, A.; Aihara, N.; Usui, K.; Torigoe, K. *Langmuir* **1998**, *14*, 3157−3159.
(19) Chechik, V.; Zhao, M.; Crooks, R. M. *J. Am. Chem. Soc.* **1999**, *121*, 4910−4911.
(20) Garcia, M. E.; Baker, L. A.; Crooks, R. M. *Anal. Chem.* **1999**, *71*, 256−258.
(21) Beck Tan, N. C.; Balogh, L.; Trevino, S. F.; Tomalia, D. A.; Lin, J. S. *Polymer* **1999**, *40*, 2537−2545.
(22) Gröhn, F.; Bauer, B. J.; Akpalu, Y. A.; Jackson, C. L.; Amis, E. J. *Macromolecules* **2000**, *33*, 6042−6050.
(23) Niu, Y.; Yeung, L. K.; Crooks, R. M. *J. Am. Chem. Soc.* **2001**, *123*, 6840−6846.
(24) Crooks, R. M.; Zhao, M.; Sun, L.; Chechik, V.; Yeung, L. K. *Acc. Chem. Res.* **2001**, *34*, 181−190.
(25) Scott, R. W. J.; Ye, H.; Henriquez, R. R.; Crooks, R. M. *Chem. Mater.* **2003**, *15*, 3873−3878.
(26) Naka, K.; Itoh, H.; Chujo, Y. *Chem. Lett.* **2004**, *33*, 1236−1237.
(27) Scott, R. W. J.; Wilson, O. M.; Crooks, R. M. *J. Phys. Chem. B* **2005**, *109*, 692−704.
(28) Hashimoto, T.; Harada, M.; Sakamoto, N. *Macromolecules* **1999**, *32*, 6867−6870.
(29) Pontoni, D.; Narayanan, T.; Rennie, A. *Langmuir* **2002**, *18*, 56−59.
(30) Hirai, H.; Nakao, Y.; Toshima, N.; Adachi, K. *Chem. Lett.* **1976**, *5*, 905−910.
(31) Suehiro, S.; Saijo, K.; Ohta, Y.; Hashimoto, T.; Kawai, H. *Anal. Chim. Acta* **1986**, *189*, 41−56.
(32) Hashimoto, T.; Okamoto, S.; Saijo, K.; Kimishima, K.; Kume, T. *Acta Polym.* **1995**, *46*, 463−470.
(33) Hendricks, R. W. *J. Appl. Crystallogr.* **1972**, *5*, 315−324.
(34) Bazzicalupi, C.; Bencini, A.; Cohen, H.; Giorgi, C.; Golub, G.; Meyerstein, D.; Navon, N.; Paoletti, P.; Valtancoli, B. *J. Chem. Soc., Dalton Trans.* **1998**, *10*, 1625−1632.
(35) Niu, Y.; Crooks, R. M. *Chem. Mater.* **2003**, *15*, 3463−3467.
(36) Esumi, K.; Nakamura, R.; Suzuki, A.; Torigoe, K. *Langmuir* **2000**, *16*, 7842−7846.
(37) Joint Committee on Powder Diffraction Standards. *Diffraction Data File*; JCPDS International Center for Diffraction Data, Newton Square, PA, 1991.
(38) Naka, K.; Itoh, H.; Chujo, Y. *Nano Lett.* **2002**, *2*, 1183−1186.
(39) Tanaka, H.; Koizumi, S.; Hashimoto, T.; Itoh, H.; Naka, K.; Chujo, Y. Manuscript in preparation.
(40) Vonk, C. G. *J. Appl. Crystallogr.* **1973**, *6*, 81−86.
(41) Hashimoto, T.; Tanaka, H.; Koizumi, S.; Itoh, H.; Naka, K.; Chujo, Y. *J. Appl. Crystallogr.* **2007**, *40*, s73−s77.
(42) Guinier, A.; Fournet, G. *Small-Angle Scattering of X-rays*; Wiley: New York, 1955.
(43) Glatter, O.; Kratky, O. *Small-Angle X-ray Scattering*; Academic Press: London, 1982.
(44) Debye, P.; Bueche, A. M. *J. Appl. Phys.* **1949**, *20*, 518−525.
(45) Porod, G. *Kolloid-Z.* **1951**, *124*, 83−114; **1952**, *125*, 51−57, 108−122.
(46) Maiti, P. K.; Çagin, T.; Wang, G.; Goddard, W. A., III. *Macromolecules* **2004**, *37*, 6236−6254.

MA062930U